Supporting Information

Large Area 23%-Efficient Monolithic Perovskite/Homojunction-Silicon Tandem Solar Cell with Enhanced UV Stability Using Down-Shifting Material

Jianghui Zheng,[*,†] Hamid Mehrvarz,[†] Chwenhaw Liao,[†] Jueming Bing,[†] Xin Cui,[†] Yang Li,[†] Vinicius R. Gonçales,[‡] Cho Fai Jonathan Lau,[†] Da Seul Lee,[†] Yong Li,[†] Meng Zhang,[†] Jincheol Kim,[†] Yongyoon Cho,[†] Laura Granados Caro,[†] Shi Tang,[†] Chao Chen,[§] Shujuan Huang,[†,ǁ] and Anita W. Y. Ho-Baillie[*,†,ǁ]

[†]Australian Centre for Advanced Photovoltaics, School of Photovoltaic and Renewable Energy Engineering, University of New South Wales, Sydney 2052, Australia
[‡] School of Chemistry, University of New South Wales, Sydney 2052, Australia
[§] College of Energy, Xiamen University, Xiamen, 361005, China
[ǁ] School of Engineering, Macquarie University, Sydney 2109, Australia

[*]Corresponding Author:
Email: a.ho-baillie@unsw.edu.au (A. Ho-Baillie), jh.zheng@unsw.edu.au (J. Zheng)

Experimental Section

Antireflective down-shifting layer preparation

The commercially available green emitting phosphor $(Ba,Sr)_2SiO_4:Eu^{2+}$ was purchased from Intematix Photonics (Shenzhen) Co., Ltd. The phosphor was firstly ground using an agate mortar and pestel for 5 min to avoid powder agglomeration.

For the fabrication of down-shifting anti-reflective PDMS layer, the liquid PDMS and a curing agent (Sylgard 184 Silicon Elastomer from Dow Corning) were mixed with 10:1 weight ratio. The phosphor powder was then added to the mixture of liquid PDMS and curing agent with the weight ratio of 0, 0.5, 1 and 3% (refer to DS0, DS0.5, DS1 and DS3 for the final PDMS film), respectively. After the phosphor incorporated PDMS was well mixed, the mixture was applied onto the surface of a textured silicon to replicate the pyramidal features onto the PDMS. The thickness of the final PDMS layer is controlled by the amount of liquid PDMS and the final thickness of the PDMS layer is around 0.3 mm. The PDMS layers were then left in air at room temperature for 48h to solidify.

Device fabrication

A double-sided polished, floating zone (FZ) 1-5 Ω-cm n-type <100>Si wafer with a thickness of 300 μm was used to prepare a bottom silicon cell. A localized heavy phosphorous ($POCl_3$) diffusion (n++) was formed for the rear contacts and a phosphorus diffused n+ high-low junction was formed on the rear side. Boron (BBr_3) diffused p++

emitter (~ 15 ohms/sq) was formed on the front and was well defined to define the active area of 4 cm^2. Metal contacts on the rear consists of Ti/Pd/Ag. The rest of the non-contacted rear was passivated by thermally grown and annealed SiO_2.[1] These silicon solar cells with a planar and un-passivated p++ front were then directly used as a substrate for the fabrication of the top perovskite cell. To complete full tandem fabrication, the surface of front polished silicon solar cells were treated by UVO cleaner for 6 min before SnO_2 electron transport layer (ETL) deposition. The SnO_2 colloidal precursor (Alfa Aesar, tin(IV) oxide, 15% in H_2O colloidal dispersion) was diluted with H_2O to 3.75%). Then, the diluted SnO_2 colloidal precursor was directly spin coated on the front of the silicon solar cells at 3000 rpm for 30 s, followed by baking on a hotplate at 150 ^oC for 30 min in the air to form a compact SnO_2 ETL. After cooling down, the SnO_2 coated silicon substrates were directly transferred to the N_2 filled glovebox for the fabrication of perovskite absorber. To prepare perovskite precursor solution, formamidinium iodide (FAI, 1 M, GreatCell Solar), lead iodide (PbI_2, 1.1 M, Alfa Aesar), methylammonium bromide (MABr, 0.2 M, GreatCell Solar), and lead bromide ($PbBr_2$, 0.2 M, Sigma-Aldrich) were dissolved in a mixed solvent of N,N-dimethylformamide (DMF, Sigma-Aldrich) and dimethyl sulfoxide (DMSO, Alfa Aesar) (4:1 v/v). The precursor was spin-coated on SnO_2 covered Si bottom cell at 2000 rpm for 20s (with the acceleration of 400 rpm/s), followed by 6000 rpm for 30s. During the spin-coating, 200 μl chlorobenzene (Sigma-Aldrich) was quickly dispensed 5 s prior

to the end of the spin process. The film was annealed at 100 ºC for 20 min producing a dark brown dense perovskite film.

For the deposition of hole transport layer (HTL), 2,2',7,7'-tetrakis(N,N-di-p-methoxyphenylamine)-9,9-spirobifluorene (spiro-OMeTAD) precursor was firstly prepared by dissolving 72.3 mg spiro-OMeTAD (Lumtec), 28.8 μL, 4-tert-butylpyridine (Sigma-Aldrich), 17.4 μL lithium bis(trifluoromethylsulphonyl)imide (Sigma-Aldrich) solution (520 mg/mL in acetonitrile (Sigma-Aldrich)) and 8 μL FK209-cobalt(III)-TFSI (GreatCell Solar) solution (300 mg of FK209-cobalt(III)-TFSI in 1 ml of acetonitrile (Sigma-Aldrich)) in 1 mL chlorobenzene (Sigma-Aldrich). The spiro-OMeTAD precursor was then deposited onto the perovskite layer by spin-coating at 3500 rpm for 30 s.

For the front transparent electrode, 18 nm of MoO_x was deposited on the spiro-OMeTAD by thermal evaporation at a rate of 0.6 Å s^{-1} under vacuum at 1×10^{-5} mTorr. The transparent contact was then fabricated by sputtering 100 nm of ITO on the MoO_x layer with a 30 W of RF power with Ar at 1.5 mTorr for 150 min using an AJA International sputtering system. A metal frame of silver was deposited by thermal evaporation to a thickness of 230 nm defining the area of the cell to 4 cm^2 aligning well with the boron diffused p++ emitter area of the bottom silicon cell.

The $(Ba,Sr)_2SiO_4:Eu^{2+}$ phosphor incorporated textured PDMS layer was then applied on the top of the tandem device for down-shifting and light trapping.

Measurements

The crystalline phase of the $(Ba,Sr)_2SiO_4:Eu^{2+}$ powder was verified by X-ray diffraction (XRD) patterns using Panalytical X-Pert PRO diffractometer with a Cu Kα (40.0 KV, 30.0 mA) radiation (λ = 0.1541 nm) at 45 kV and 40 mA.

Phosphor morphology, device film top view, cross-sectional scanning electron microscopy (SEM) images and elemental distribution across the phosphor sample were obtained using a field emission SEM (NanoSEM 450) equipped with energy dispersive X-ray spectroscopy system. To observe the phosphor distribution in the PDMS film, the top morphology of PDMS film also observed by a laser microscope (VK-X200, Keyence, Osaka, Japan).

X-ray photoelectron spectroscopy (XPS) was carried out using ESCALAB250Xi, Thermo Scientific, UK.

Photoluminescence excitation (PLE) and emission (PL) spectra of phosphor powder sample and luminescence thin films were measured by Hitachi F-7000 spectrofluorometer equipped with a 150 W Xenon lamp as an excitation source.

The absolute photoluminescence quantum yield (PLQY) of phosphor was measured using a standard Edinburgh Instruments FLS980 spectrometer equipped with an integrating sphere attachment (excited by 365 nm). The absolute PLQY is calculated by the following equation: [2]

$$\eta_{PLQY} = \frac{\int L_s}{\int E_R - \int E_s} \quad (2)$$

where L_S is the luminescence emission spectrum of the phosphor sample; E_S is the spectrum of the light used for exciting the phosphor sample; E_R is the spectrum of the excitation light without the sample in the integrating sphere.

The PL decay traces were measured by Microtime200 microscope (Picoquant) using time-correlated single photon counting (TCSPC) technique with excitation of 470 nm laser at 5 MHz repetition rate and detection through 500 nm band-pass filter.

The optical reflection and transmission spectra were measured using Perkin Elmer Lambda1050 UV/Vis/NIR spectrophotometer.

The current density-voltage (*J*–*V*) measurements of tandem devices were performed using a solar cell *I*–*V* testing system from Abet Technologies, Inc. (using class AAA solar simulator) under an illumination power of 100 mW cm^{-2} with metal aperture of 4cm^2 and a scan rate of 30 mV s^{-1} from open-circuit voltage (V_{OC}) to short-circuit current density (J_{SC}) direction (1.8 V to -0.1 V). The *J*-*V* curves of best tandem devices were also measured with the forward scan by a scan rate of 30 mV s^{-1} from J_{SC} to V_{OC} direction (-0.1 V to 1.8 V). The light was calibrated using a certified reference cell. The bias voltage for the steady-state measurements was chosen as the average of maximum power point (MPP) voltage of the *J*-*V* measurement.

The external quantum efficiency (EQE) measurement of tandem devices was carried out using the PV Measurement QXE7 Spectral Response system with monochromatic light from a xenon arc lamp and with a chopping frequency of 120 Hz. The EQE response

was calibrated using two certified reference cells for 300-1000 nm and 1000-1400 nm wavelength regions, respectively. The blue LED light (450 nm) and near-infrared LED light (850 nm) was used to saturate (where current reading > 0) the top and the bottom cell for the EQE measurement of the bottom silicon cell and top perovskite cell, respectively. Bias light intensity within the range of 35 to 800 lux is suitable without affecting the saturation of each subcell.

Contact angle measurements of PDMS films were conducted with a Ramé-hart contact angle goniometer (Model 200) and the corresponding contact angles were calculated using DROPimage standard software.

The tensile tests were carried out using an Instron-5500 electronic universal test machine measured in air, with a crosshead speed of 5 mm/min.

WFH-203B multi-functional UV box analyzer (Shanghai Chitang) was used to carry out UV stability testing for the tandem devices. The UV light intensity was calibrated to 5 mW/cm^2 by TM-231 UV-AB Meter (Tenmars).

All cell measurements were undertaken at room temperature in ambient condition.

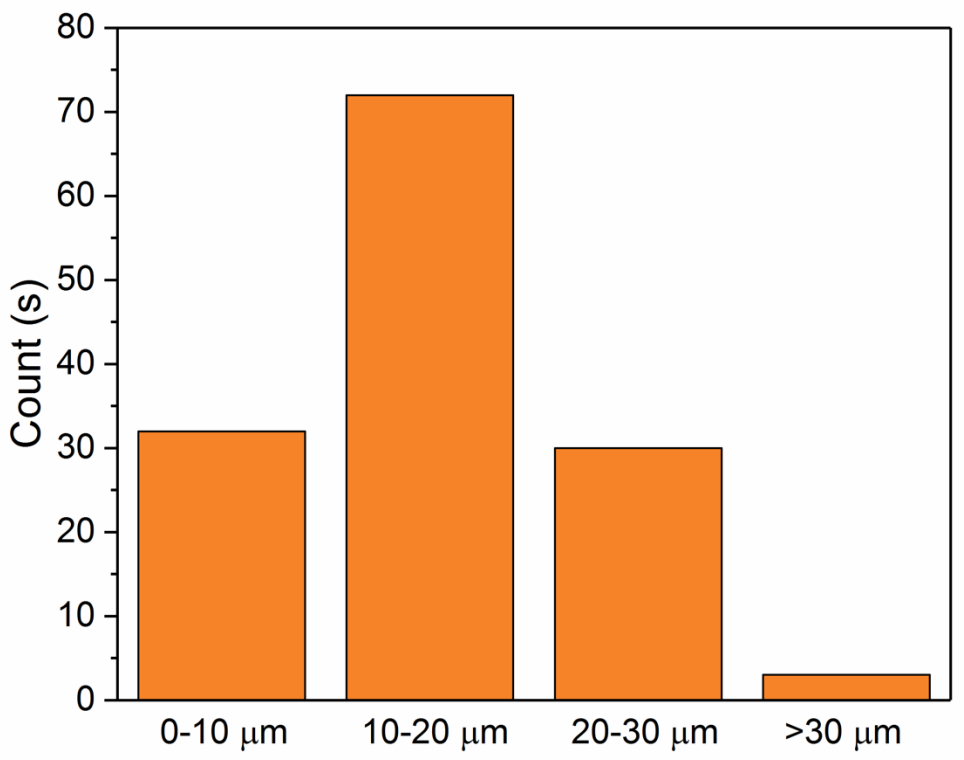

Figure S1 Size distribution of $(Sr,Ba)_2SiO_4:Eu^{2+}$ phosphors

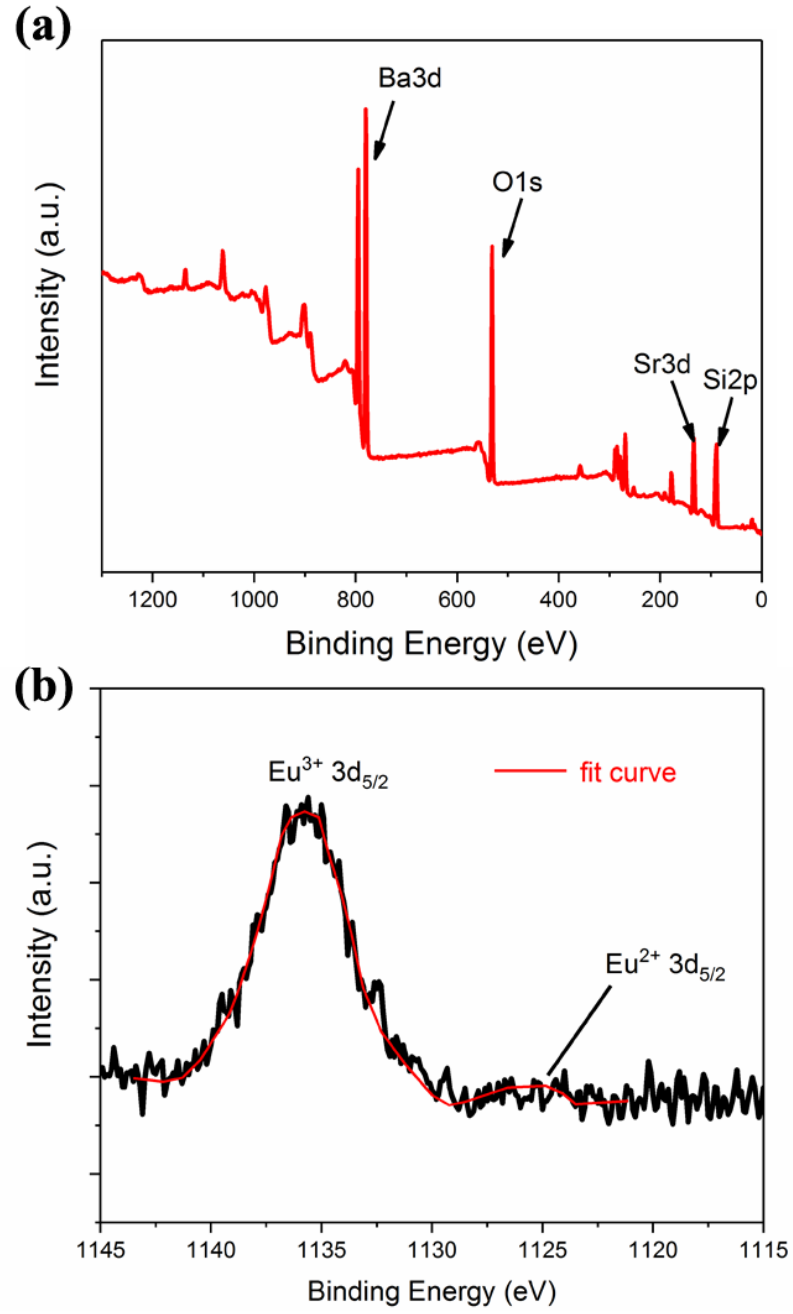

Figure S2 a) XPS measurement of $(Sr,Ba)_2SiO_4:Eu^{2+}$ phosphor. b) XPS spectra of the $Eu3d_{5/2}$ core level.

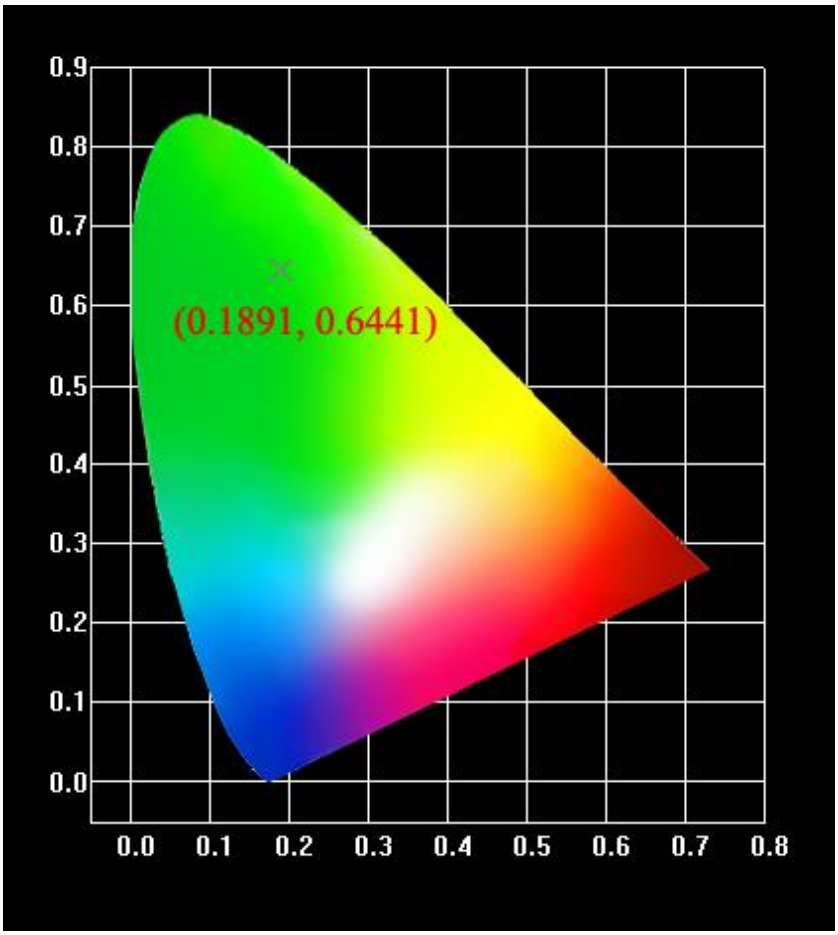

Figure S3 CIE chromaticity coordinate diagram of $(Sr,Ba)_2SiO_4:Eu^{2+}$ phosphor

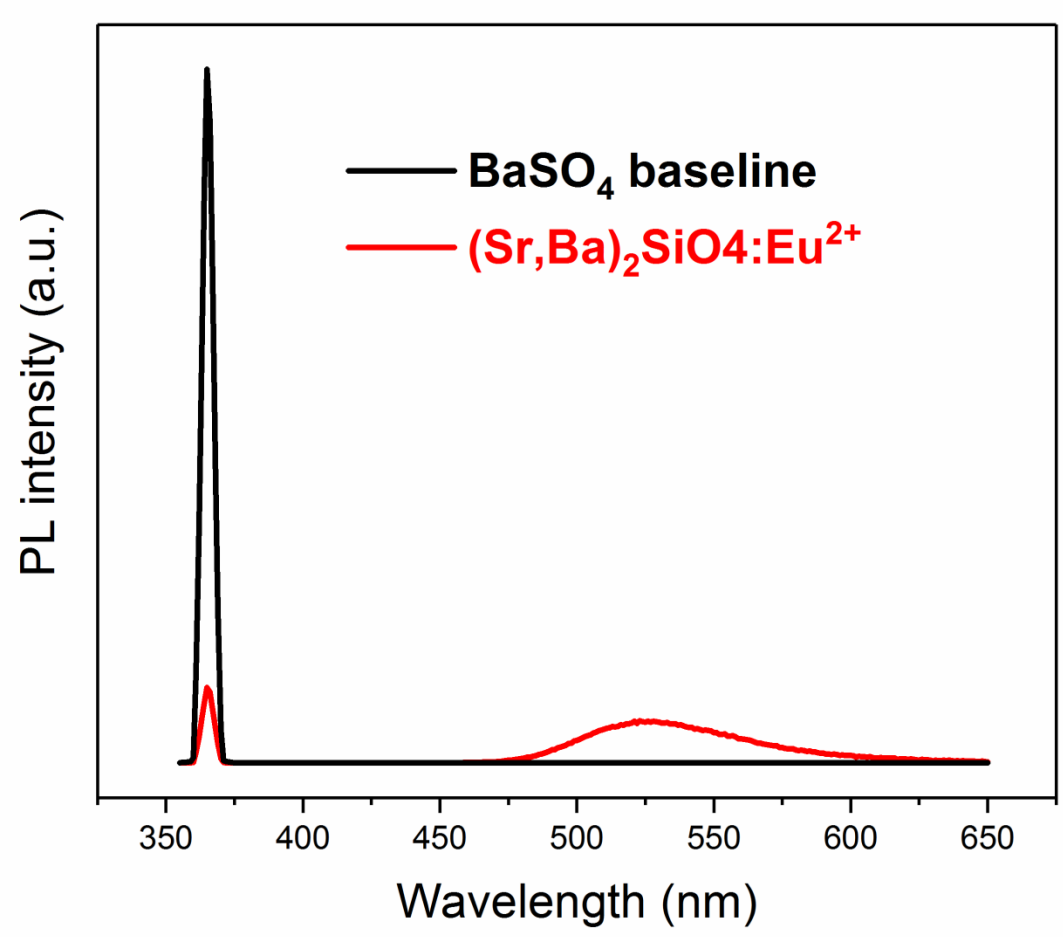

Figure S4 PLQY measurement of $(Sr,Ba)_2SiO_4:Eu^{2+}$ phosphor.

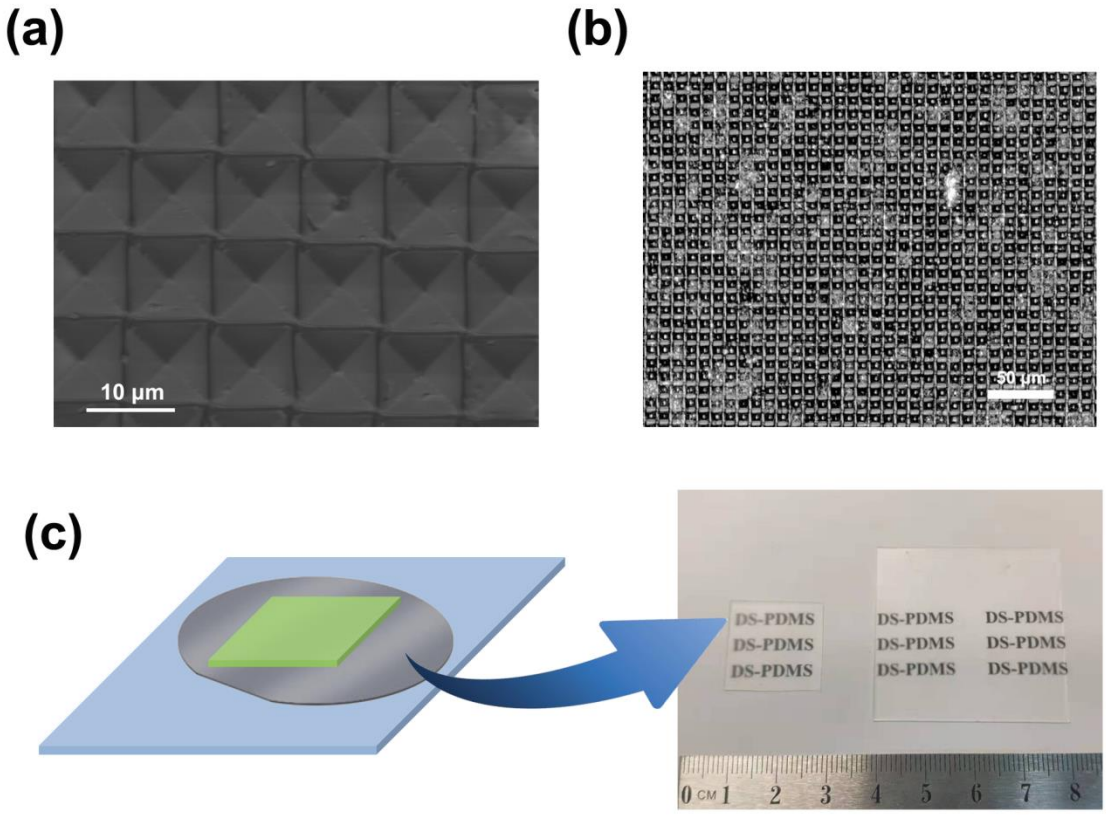

Figure S5 Top view (a) SEM, (b) optical microscope images of the textured surfaces of DS0.5 PDMS layer. (c) Illustration of using textured Si wafer as a mould for the fabrication of PDMS and photo shows the fabricated PDMS on large area.

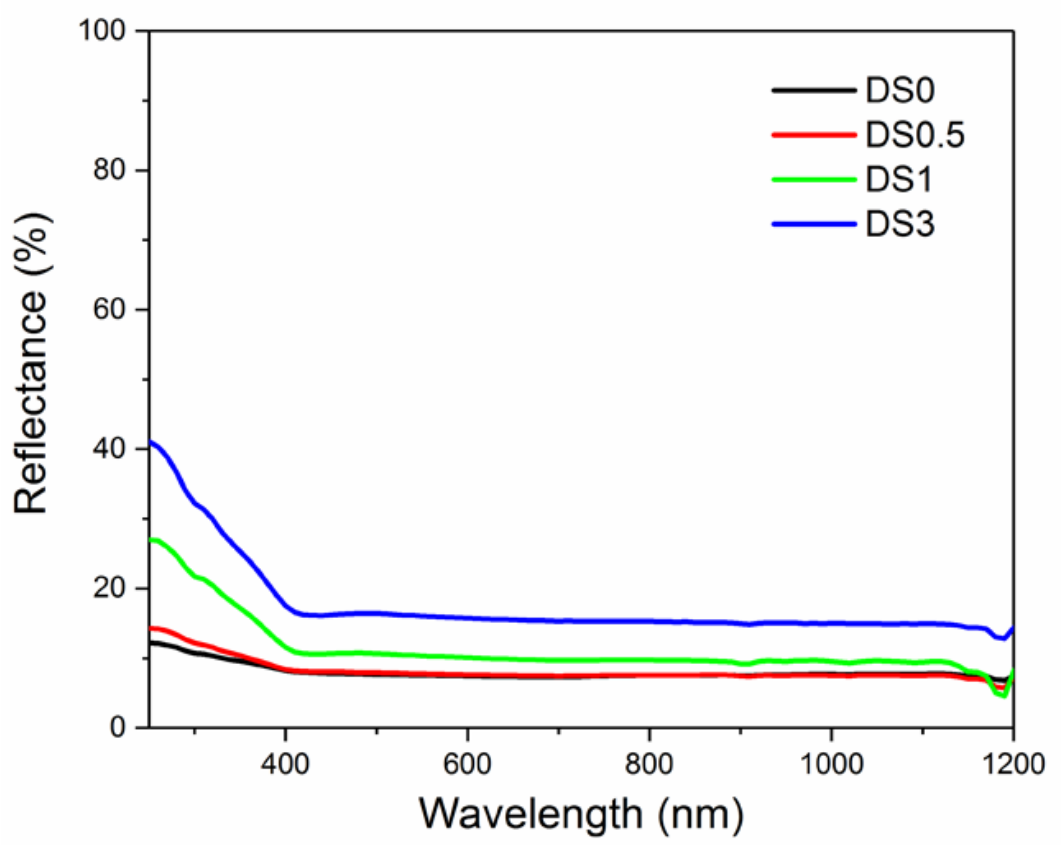

Figure S6 Reflectance measured for DS0, DS0.5, DS1 and DS3 PDMS films.

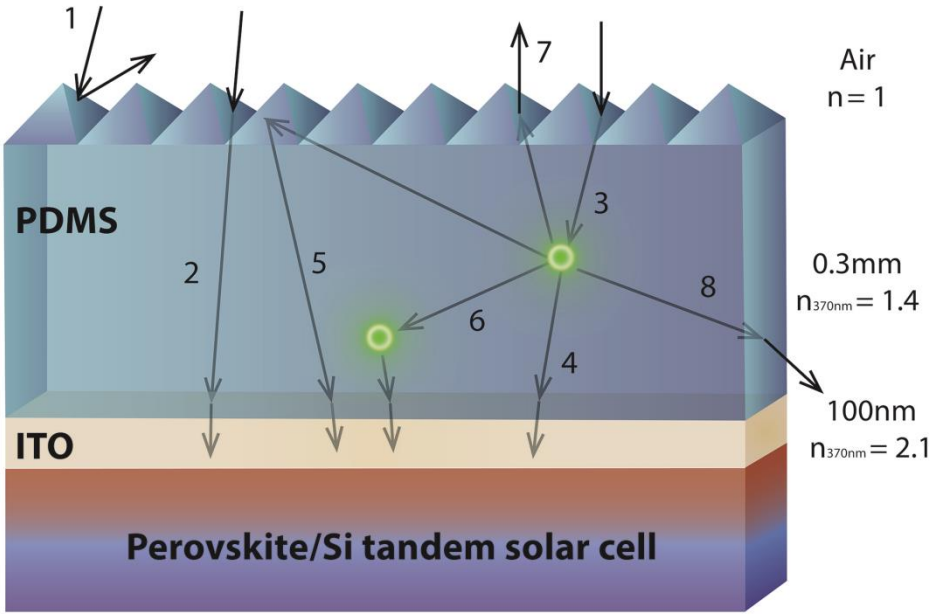

Figure S7. Illustration of possible optical pathways for tandem cell with front down-shifting PDMS antireflection layer. Reflected by the textured PDMS surface (1); Either part of short- λ or long- λ light direct entering the ITO layer of tandem device (2); Part of short- λ will be absorbed by the micro phosphor (3) and reemitted the green light directly into the the ITO layer of tandem device (4) or after the textured surface internal re-emission into the ITO layer of tandem device (5), or re-absorbed and re-emitted by the another micro phosphor (6), or escape out from the PDMS textured surface (7) or the sides (8).

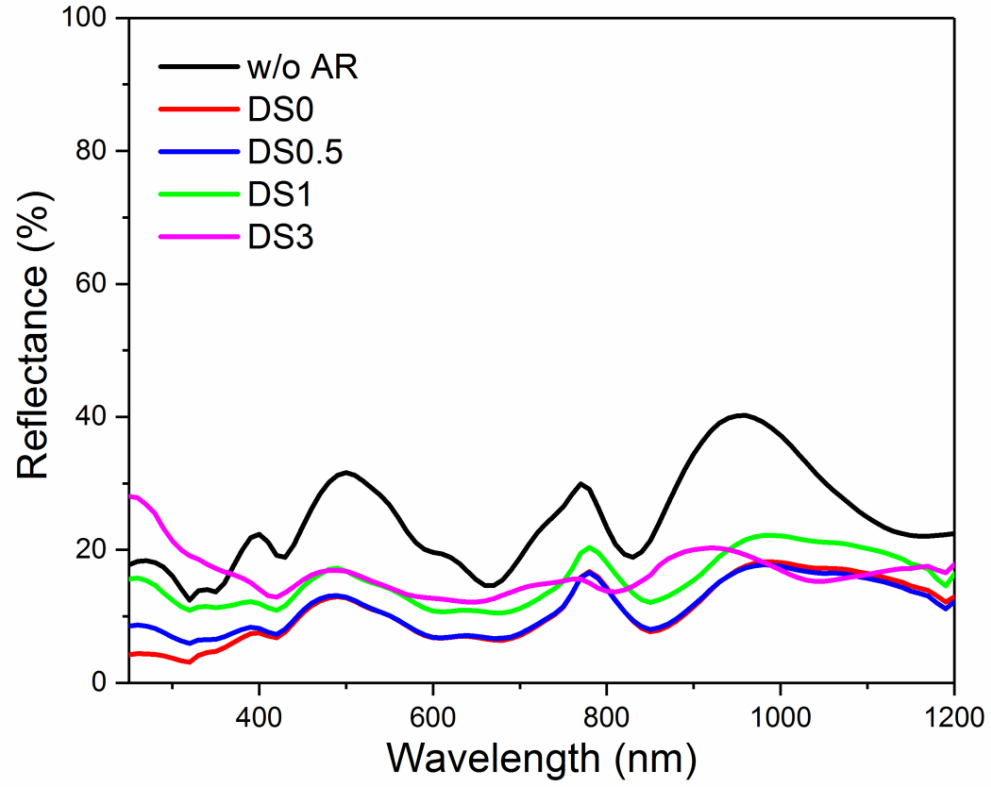

Figure S8 Reflectance of baseline (without AR), DS0, DS0.5, DS1 and DS3 tandem devices.

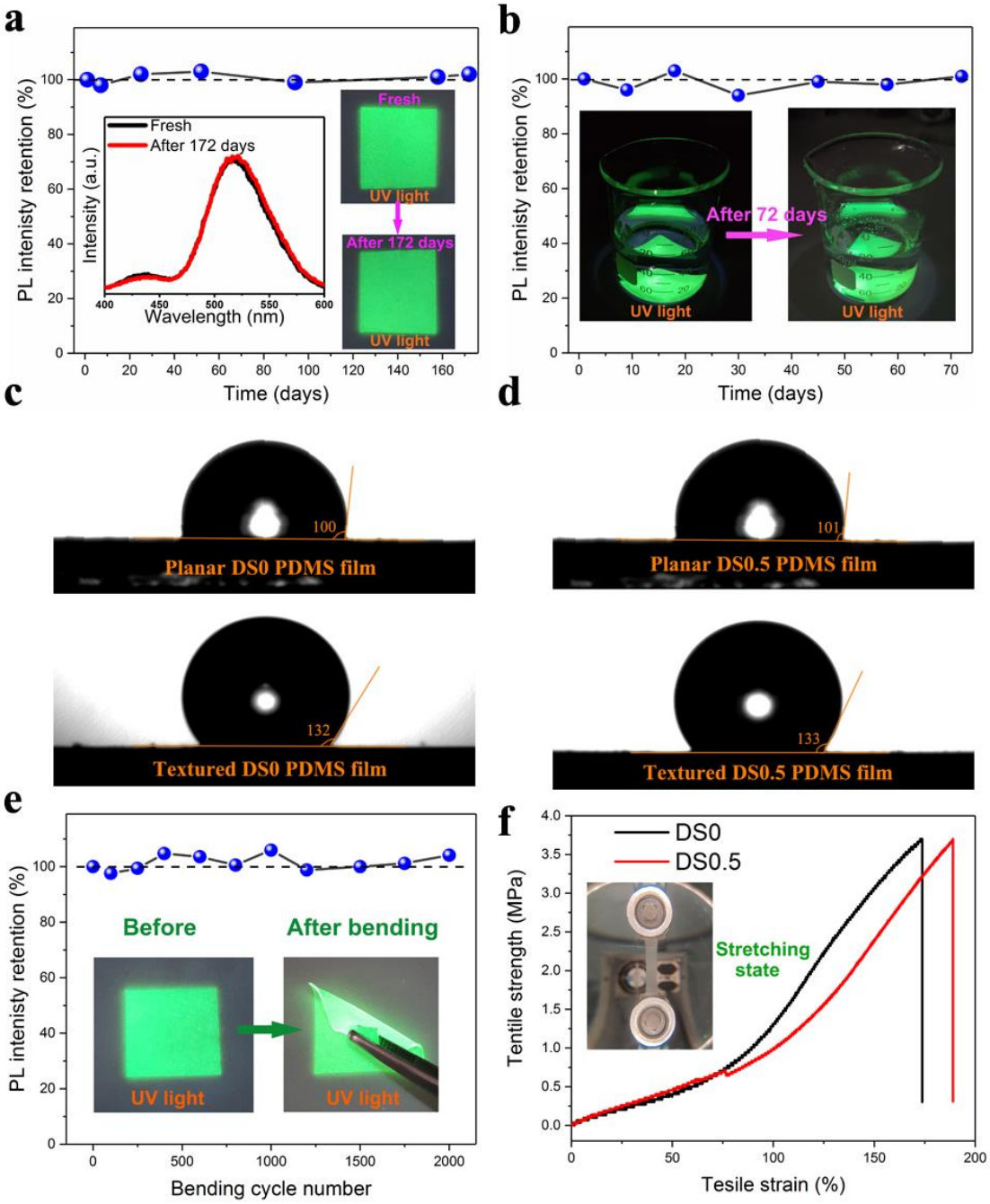

Figure S9: PL intensity evolution and of DS0.5film during storage (inset: photos of films under UV light before and after) (a) in air (temperature of 25 °C and relative humidity of 50%) for 172 days b) in water for 72 days. Water contact-angle measurement of planar and textured c) DS0 and d) DS0.5 films. e) PL intensity evolution of the DS0.5 film during 2000 cycles of bending test (inset: photos of films under UV light before and after). f) Tensile curves of the DS0 and DS0.5 films (inset: tensile curve measurement set up).

Figure S10 Photo of UV box analyzer for UV stability test in N_2 filled glovebox. Inset: photo showing UV light intensity reading of 5 mW/cm^2 on a UV Meter.

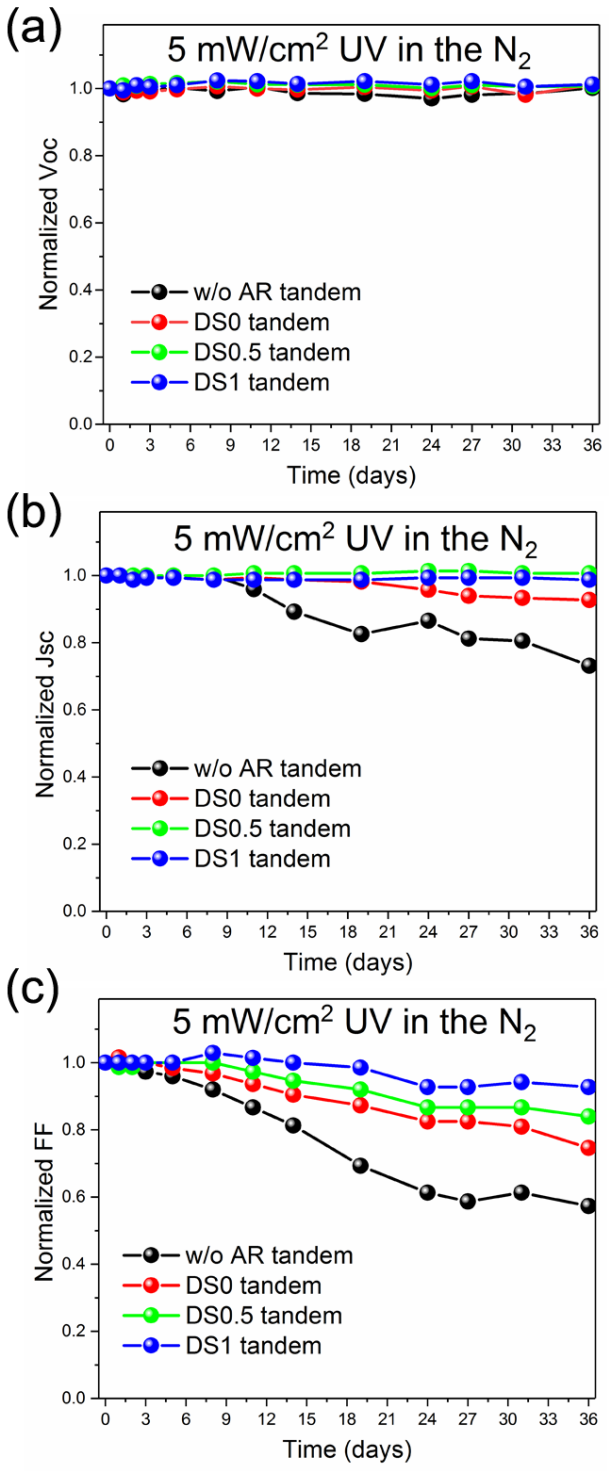

Figure S11 Evolution of V_{OC}, J_{SC} and FF of baseline tandem (w/o AR), DS0 tandem, DS0.5 tandem and DS1 tandem devices during the 5 mW/cm^2 UV light testing in N_2.

Table S1 Summaries of monolithic 2-terminal perovskite/silicon tandem device.

Perovskite	Eg (eV)	Silicon	Interface layer	V_{OC} (V)	J_{SC} (mA/cm^2)	*FF*	PCE (%)	Steady-state or certified PCE (%)	Area (cm^2)	Institute	Publish month and Ref
$MAPbI_3$	1.55	Homojunction	n++ Si	1.58	11.5	0.75	-	13.7	1.00	MIT/Stanford	2015.03 [3]
$MAPbI_3$	1.55	Homojunction	ZTO	1.64	15.3	0.65	16.3	16.0	1.43	EPFL	2016.12 [4]
$CsRbFAMAPbI_{3-x}Br_x$	1.62	Homojunction	ITO	1.75	17.6	0.74	22.8	22.5	1.00	ANU	2017.10 [5]
$MAPbI_3$	1.58	Homojunction	-	1.68	16.1	0.78	21.0	20.5	4.00	UNSW	2018.06 [6]
$MAPbI_3$	1.58	Homojunction	-	1.66	15.6	0.68	17.6	17.1	16.00		
$FAMAPbI_{3-x}Br_x$	1.59	Homojunction	-	1.74	16.2	0.78	21.9	21.8	16.00	UNSW	2018.08 [7]
$CsRbFAMAPbI_{3-x}Br_x$	1.62	Homojunction	-	1.70	17.2	0.79	23.2	22.9	1.00	ANU	2018.12 [8]
$FAMAPbI_{3-x}Br_x$	1.64	Homojunction	ITO	1.65	16.1	0.80	21.2	21.1	0.27	UNIST	2019.03 [9]
$FAMAPbI_{3-x}Br_x$	**1.61**	**Homojunction**	-	**1.73**	**16.5**	**0.81**	**23.1**	**23.0**	**4.00**	**UNSW**	**This work**
$FAMAPbI_{3-x}Br_x$	1.56	SHJ	ITO	1.79	14.0	0.77	19.1	18.1	0.16	HZB/EPFL	2015.10 [10]
$MAPbI_3$	1.55	SHJ	IZO	1.69	15.9	0.78	20.9	21.2	0.17	EPFL	2015.12 [11]
$MAPbI_3$	1.55	SHJ	IZO	1.70	16.1	0.71	19.5	19.2	1.22		
$MAPbI_3$	1.55	SHJ	IZO	1.72	16.4	0.73	20.6	20.5	1.43	EPFL	2016.07 [12]
$CsFAPbI_{3-x}Br_x$	1.63	SHJ	ITO	1.65	18.1	0.79	23.6	23.6*****	1.00	Stanford	2017.02 [13]
$CsFAPbI_{3-x}Br_x$	1.63	SHJ	nc-Si	1.75	16.8	0.76	22.8	22.0	0.25	EPFL	2017.08 [14]
$CsFAPbI_{3-x}Br_x$	1.63	SHJ	nc-Si	1.78	16.5	0.74	21.8	21.2	1.43		
$CsFAPbI_{3-x}Br_x$	1.63	SHJ	nc-Si	1.77	16.5	0.65	19.1	18.0	12.96		
$FAMAI_{3-x}Br_x$	1.69	SHJ	ITO	1.7	15.3	0.79	20.6	18.0	0.03	PKU	2017.10 [15]
$FAMAPbI_{3-x}Br_x$	N/P	SHJ	ITO	1.71	15.5	0.71	18.8	N/P	0.13	NKU	2017.12 [16]
$CsFAPbI_{3-x}Br_x$	1.63	SHJ	ITO	1.79	19.5	0.72	25.5	25.2*****	1.419	EPFL	2018.06 [17]
$CsFAMAPbI_{3-x}Br_x$	1.63	SHJ	ITO	1.79	19.0	0.73	25.4	25.2*****	1.088	HZB/Oxford PV	2018.06 [18]
N/P	N/P	SHJ	N/P	1.80	19.8	0.79	28.0	28.0*****	1.03	Oxford PV	2018.06 [19]

$CsFAPbI_{3-x}Br_x$	1.63	SHJ	ITO	1.77	18.4	0.77	25.0	N/P	1.00	Stanford	2018.08 [20]
$CsFAMAPbI_{3-x}Br_x$	1.69	SHJ	ITO	1.66	16.5	0.81	22.2	N/P	0.06	PKU	2018.10 [21]
$CsFAMAPbI_{3-x}Br_x$	1.65	SHJ	ITO	1.78	17.1	0.74	22.8	N/P	0.13	NKU	2018.10 [22]
$CsFAMAPbI_{3-x}Br_x$	1.64	SHJ	ITO	1.80	17.8	0.79	25.4	N/P	0.422	UNL	2018.10 [23]
$CsFAMAPbI_{3-x}Br_x$	N/P	SHJ	ITO	1.76	18.5	0.79	25.5	N/P	0.81	HZB	2018.10 [24]
$CsFAMAPbI_{3-x}Br_x$	N/P	SHJ	ITO	1.75	16.9	0.74	21.9	N/P	0.13	NKU	2018.11 [25]
$CsRbFAMAPbI_{3-x}Br_x$	1.62	SHJ (poly-Si)	-	1.76	17.8	0.78	24.5	24.1	1.00	ANU	2018.12 [8]
$CsFAMAPbI_{3-x}Br_x$	1.67	SHJ	ITO	1.83	16.0	0.70	20.4	N/P	0.13	NKU	2019.01 [26]
$CsFAPbI_{3-x}Br_x$	1.63	SHJ ($nc\text{-}SiC_x$)	nc-Si	1.74	19.5	0.75	25.4	25.1	1.43	EPFL	2019.03 [27]
$CsFAPbI_{3-x}Br_x$	1.63	SHJ	ITO	1.72	17.5	0.75	22.6	22.6	57.4	CSEM/EPFL	2019.04 [28]
$CsFAMAPbI_{3-x}Br_x$	1.59	SHJ	ITO	1.76	19.2	0.77	26.0	26.0	0.77	HZB	2019.05 [29]

*****certified by NREL or Fraunhofer. N/P: not reported.

Acronyms:

MIT: Massachusetts Institute of Technology, USA
Stanford: Stanford University, USA
EPFL: École polytechnique fédérale de Lausanne, Switzerland
ANU: The Australian National University, Australia
UNIST: Ulsan National Institute of Science and Technology, South Korea
UNSW: The University of New South Wales, Australia
HZB: Helmholtz-Zentrum Berlin, Germany
PKU: Peking University, China
NKU: Nankai University, China
Oxford PV: Oxford Photovoltaics Limited, UK
UNL: University of Nebraska–Lincoln, USA
CSEM: The Swiss Center for Electronics and Microtechnology, Switzerland

Reference:

1. Zhao, J .; Wang, A.; Green, M. A. 24.5% Efficiency Silicon PERT Cells on MCZ Substrates and 24.7% Efficiency PERL cells on FZ Substrates. *Prog. Photovolt: Res. Appl.*, **1999**, *7*, 471-474.
2. Zhao, M.; Liao, H.; Ning, L.; Zhang, Q.; Liu, Q.; Xia, Z. Next-Generation Narrow-Band Green-Emitting $RbLi(Li_3SiO_4)_2$:Eu^{2+} Phosphor for Backlight Display Application. *Adv. Mater.*, **2018**, *38*, 1802489.
3. Mailoa, J. P.; Bailie, C. D.; Johlin, E. C.; Hoke, E. T.; Akey, A. J.; Nguyen, W. H.; McGehee, M. D.; Buonassisi, T. A 2-terminal Perovskite/silicon Multijunction Solar Cell Enabled by a Silicon Tunnel Junction. *Appl. Phys. Lett.*, **2015**, *106*, 121105.
4. Werner, J.; Walter, A.; Rucavado, E.; Moon, S.-J.; Sacchetto, D.; Rienaecker, M.; Peibst, R.; Brendel, R.; Niquille, X.; De Wolf, S.; Löper, P.; Morales-Masis, M.; Nicolay, S.; Niesen, B.; Ballif, C. Zinc Tin Oxide as High-Temperature Stable Recombination layer for Mesoscopic Perovskite/Silicon Monolithic Tandem Solar Cells. *Appl. Phys. Lett.*, **2016**, *109*, 233902.
5. Wu, Y.; Yan, D.; Peng, J.; Duong, T.; Wan, Y.; Phang, P.; Shen, H.; Wu, N.; Barugkin, C.; Fu, X.; Surve, S.; Walter, D.; White, T.; Catchpole, K.; Weber, K. Monolithic Perovskite/Silicon-Homojunction Tandem Solar Cell with Over 22% Efficiency. *Energy Environ. Sci.*, **2017**, *10*, 2472-2479.
6. Zheng, J.; Lau, C. F. J.; Mehrvarz, H.; Ma, F.-J.; Jiang, Y.; Deng, X.; Soeriyadi, A.; Kim, J.; Zhang, M.; Hu, L.; Cui, X.; Lee, D. S.; Bing, J.; Cho, Y.; Chen, C.; Green, M. A.; Huang, S.; Ho-Baillie, A. W. Y. Large Area Efficient Interface Layer Free Monolithic Perovskite/Homo-Junction-Silicon Tandem Solar Cell with over 20% Efficiency. *Energy Environ. Sci.*, **2018**, *11*, 2432-2443.
7. Zheng, J.; Mehrvarz, H.; Ma, F.-J.; Lau, C.-F. J.; Green, M.; Huang, S.; Ho-Baillie, A. W. Y. 21.8% Efficient Monolithic Perovskite/Homo-Junction-Silicon Tandem Solar Cell on 16 cm^2. *ACS Energy Lett.*, **2018**, *3*, 2299-2300.
8. Shen, H.; Omelchenko, S. T.; Jacobs, D. A.; Yalamanchili, S.; Wan, Y.; Yan, D.; Phang, P.; Duong, T.; Wu, Y.; Yin, Y.; Samundsett, C.; Peng, J.; Wu, N.; White, T. P.; Andersson, G. G.; Lewis, N. S.; Catchpole, K. R. In Situ Recombination Junction Between p-Si and TiO_2 Enables High-Efficiency Monolithic Perovskite/Si Tandem Cells. *Sci. Adv.*, **2018**, *4*, eaau9711.
9. Kim, C. U.; Yu, J. C.; Jung, E. D.; Choi, I. Y.; Park, W.; Lee, H.; Kim, I.; Lee, D.-K.; Hong, K. K.; Song, M. H. Optimization of Device Design for Low Cost and High Efficiency Planar Monolithic Perovskite/Silicon Tandem Solar Cells. *Nano Energy*, **2019**, *60*, 213-221.
10. Albrecht, S.; Saliba, M.; Correa Baena, J. P.; Lang, F.; Kegelmann, L.; Mews, M.; Steier, L.; Abate, A.; Rappich, J.; Korte, L.; Schlatmann, R.; Nazeeruddin, M. K.; Hagfeldt, A.; Grätzel, M.; Rech, B. Monolithic Perovskite/Silicon-Heterojunction

Tandem Solar Cells Processed at Low Temperature. *Energy Environ. Sci.*, **2016**, *9*, 81-88.

11. Werner, J.; Weng, C. H.; Walter, A.; Fesquet, L.; Seif, J. P.; De Wolf, S.; Niesen, B.; Ballif, C. Efficient Monolithic Perovskite/Silicon Tandem Solar Cell with Cell Area >1 cm^2. *J. Phys. Chem. Lett.*, **2016**, *7*, 161-166.
12. Werner J.; Barraud L.; Walter A.; Bräuninger M.; Sahli F.; Sacchetto D.; Tétreault N.; Paviet-Salomon B.; Moon SJ.; Allebé C.; Despeisse M.; Nicolay S.; Wolf De S.; Niesen B.; Ballif C. Efficient Near-Infrared-Transparent Perovskite Solar Cells Enabling Direct Comparison of 4-Terminal and Monolithic Perovskite/Silicon Tandem Cells, *ACS Energy Lett*., **2016**, *1*, 474-480.
13. Bush, K. A.; Palmstrom, A. F.; Yu, Z. J.; Boccard, M.; Cheacharoen, R.; Mailoa, J. P.; McMeekin, D. P.; Hoye, R. L. Z.; Bailie, C. D.; Leijtens, T.; Peters, I. M.; Minichetti, M. C.; Rolston, N.; Prasanna, R.; Sofia, S.; Harwood, D.; Ma, W.; Moghadam, F.; Snaith, H. J.; Buonassisi, T.; Holman, Z. C.; Bent, S. F.; McGehee, M. D. 23.6%-Efficient Monolithic Perovskite/Silicon Tandem Solar Cells with Improved Stability. *Nature Energy*, **2017**, *2*, 17009.
14. Sahli, F.; Kamino, B. A.; Werner, J.; Bräuninger, M.; Paviet-Salomon, B.; Barraud, L.; Monnard, R.; Seif, J. P.; Tomasi, A.; Jeangros, Q.; Hessler-Wyser, A.; De Wolf, S.; Despeisse, M.; Nicolay, S.; Niesen, B.; Ballif, C. Improved Optics in Monolithic Perovskite/Silicon Tandem Solar Cells with a Nanocrystalline Silicon Recombination Junction. *Adv. Energy Mater.*, **2018**, *8*, 1701609.
15. Fan, R.; Zhou, N.; Zhang, L.; Yang, R.; Meng, Y.; Li, L.; Guo, T.; Chen, Y.; Xu, Z.; Zheng, G.; Huang, Y.; Li, L.; Qin, L.; Qiu, X.; Chen, Q.; Zhou, H. Toward Full Solution Processed Perovskite/Si Monolithic Tandem Solar Device With PCE Exceeding 20%. *Sol. RRL*, **2017**, *1*, 1700149.
16. Zhu, S.; Yao, X.; Ren, Q.; Zheng, C.; Li, S.; Tong, Y.; Shi, B.; Guo, S.; Fan, L.; Ren, H.; Wei, C.; Li, B.; Ding, Y.; Huang, Q.; Li, Y.; Zhao, Y.; Zhang, X. Transparent Electrode for Monolithic Perovskite/Silicon-Heterojunction Two-terminal Tandem Solar Cells. *Nano Energy*, **2018**, *45*, 280-286.
17. Sahli, F.; Werner, J.; Kamino, B. A.; Brauninger, M.; Monnard, R.; Paviet-Salomon, B.; Barraud, L.; Ding, L.; Diaz Leon, J. J.; Sacchetto, D.; Cattaneo, G.; Despeisse, M.; Boccard, M.; Nicolay, S.; Jeangros, Q.; Niesen, B.; Ballif, C. Fully Textured Monolithic Perovskite/Silicon Tandem Solar Cells with 25.2% Power Conversion Efficiency. *Nat. Mater.*, ***2018***, *17*, 820.
18. Mazzarella, L.; Lin, Y.-H.; Kirner, S.; Morales-Vilches, A. B.; Korte, L.; Albrecht, S.; Crossland, E.; Stannowski, B.; Case, C.; Snaith, H. J.; Schlatmann, R. Infrared Light Management Using a Nanocrystalline Silicon Oxide Interlayer in Monolithic Perovskite/Silicon Heterojunction Tandem Solar Cells with Efficiency above 25%. *Adv. Energy Mater.*, **2019**, *9*, 1803241.

19. Green, M. A.; Hishikawa, Y.; Dunlop, E. D.; Levi, D. H.; Hohl-Ebinger, J.; Yoshita, M.; Ho-Baillie, A. W. Y. Solar Cell Efficiency Tables (Version 54). *Prog. Photovoltaics*, **2019**, *27*, 565-575.
20. Bush, K. A.; Manzoor, S.; Frohna, K.; Yu, Z. J.; Raiford, J. A.; Palmstrom, A. F.; Wang, H.-P.; Prasanna, R.; Bent, S. F.; Holman, Z. C.; McGehee, M. D. Minimizing Current and Voltage Losses to Reach 25%-Efficient Monolithic Two-Terminal Perovskite-Silicon Tandem Solar Cells. *ACS Energy Lett.*, **2018**, *9*, 2173-2180.
21. Qiu, Z.; Xu, Z.; Li, N.; Zhou, N.; Chen, Y.; Wan, X.; Liu, J.; Li, N.; Hao, X.; Bi, P.; Chen, Q.; Cao, B.; Zhou, H. Monolithic perovskite/Si tandem solar cells exceeding 22% efficiency via optimizing top cell absorber. *Nano Energy*, **2018**, *53*, 798-807.
22. Zhu, S.; Hou, F.; Huang, W.; Yao, X.; Shi, B.; Ren, Q.; Chen, J.; Yan, L.; An, S.; Zhou, Z.; Ren, H.; Wei, C.; Huang, Q.; Li, Y.; Hou, G.; Chen, X.; Ding, Y.; Wang, G.; Li, B.; Zhao, Y.; Zhang, X. Solvent Engineering to Balance Light Absorbance and Transmittance in Perovskite for Tandem Solar Cells. *Sol. RRL*, **2018**, *11*, 1800176.
23. Chen, B.; Yu, Z.; Liu, K.; Zheng, X.; Liu, Y.; Shi, J.; Spronk, D.; Rudd, P. N.; Holman, Z.; Huang, J. Grain Engineering for Perovskite/Silicon Monolithic Tandem Solar Cells with Efficiency of 25.4%. *Joule*, **2019**, *3*, 177-190.
24. Jošt, M.; Köhnen, E.; Morales Vilches, A.; Lipovšek, B.; Jäger, K.; Macco, B.; Al-Ashouri, A.; Krc, J.; Korte, L.; Rech, B.; Schlatmann, R.; Topic, M.; Stannowski, B.; Albrecht, S. Textured interfaces in Monolithic Perovskite/Silicon Tandem Solar Cells: Advanced Light Management for Improved Efficiency and Energy Yield. *Energy Environ. Sci.*, **2018**, *11*, 3511-3523.
25. Hou, F.; Han, C.; Isabella, O.; Yan, L.; Shi, B.; Chen, J.; An, S.; Zhou, Z.; Huang, W.; Ren, H.; Huang, Q.; Hou, G.; Chen, X.; Li, Y.; Ding, Y.; Wang, G.; Wei, C.; Zhang, D.; Zeman, M.; Zhao, Y.; Zhang, X. Inverted pyramidally-textured PDMS antireflective foils for perovskite/silicon tandem solar cells with flat top cell. *Nano Energy*, **2019**, *56*, 234-240.
26. Hou, F.; Yan, L.; Shi, B.; Chen, J.; Zhu, S.; Ren, Q.; An, S.; Zhou, Z.; Ren, H.; Wei, C.; Huang, Q.; Hou, G.; Chen, X.; Li, Y.; Ding, Y.; Wang, G.; Zhang, D.; Zhao, Y.; Zhang, X. Monolithic Perovskite/Silicon-Heterojunction Tandem Solar Cells with Open-Circuit Voltage of over 1.8 V. *ACS Appl. Energy Mater.*, **2019**, *2*, 243-249.
27. Nogay, G.; Sahli, F.; Werner, J.; Monnard, R.; Boccard, M.; Despeisse, M.; Haug, F.-J.; Jeangros, Q.; Ingenito, A.; Ballif, C. 25.1%-Efficient Monolithic Perovskite/Silicon Tandem Solar Cell Based on a p-type Mono-crystalline Textured Silicon Wafer and High Temperature Passivating Contacts. *ACS Energy Lett.*, **2019**, *4*, 844-845.
28. Kamino, B.; Paviet-Salomon, B.; Moon, S.-J.; Badel, N.; Levrat, J.; Christmann, G.; Walter, A.; Faes, A.; Ding, L.; Diaz Leon, J. J.; Paracchino, A.; Despeisse, M.; Ballif, C.; Nicolay, S. Low Temperature Screen-Print Metallization for the Scale

Up of 2-Terminal Perovskite-Silicon Tandems. *ACS Appl. Energy Mater.*, **2019**, *2*, 3815-3821.

29. Köhnen, E.; Jošt, M.; Morales-Vilches, A. B.; Tockhorn, P.; Al-Ashouri, A.; Macco, B.; Kegelmann, L.; Korte, L.; Rech, B.; Schlatmann, R.; Stannowski, B.; Albrecht, S. Highly Efficient Monolithic Perovskite Silicon Tandem Solar Cells: Analyzing the Influence of Current Mismatch on Device Performance. *Sustain. Energy Fuels*, **2019**, *3*, 1995-2005.